Acta Materialia 165 (2019) 362–372

Contents lists available at ScienceDirect

Acta Materialia

journal homepage: www.elsevier.com/locate/actamat

Full length article

Variant selection of intragranular $Ni_2(Mo,Cr)$ precipitates (γ') in the Ni-Mo-Cr-W alloy

Jie Song [a, *], Robert Field [a], Amy Clarke [a], Yao Fu [b, **], Michael Kaufman [a]

[a] Center for Advanced Non-Ferrous Structural Alloys, Department of Metallurgical and Materials Engineering, Colorado School of Mines, 1500 Illinois Street, Golden, CO, 80401, USA
[b] Department of Aerospace Engineering and Engineering Mechanics, University of Cincinnati, 2600 Clifton Avenue, Cincinnati, OH, 45221, USA

ARTICLE INFO

Article history:
Received 16 September 2018
Received in revised form
26 November 2018
Accepted 30 November 2018
Available online 3 December 2018

Keywords:
Precipitate variant selection
Stress aided aging
$Ni_2(Mo,Cr)$ intragranular precipitation
Nickel-based superalloys
Phase field modeling

ABSTRACT

Variant selection of $Ni_2(Mo,Cr)$ precipitates (γ') in a low coefficient of thermal expansion Ni-Mo-Cr-W alloy has been investigated as a function of precipitate size and applied stress. The lenticular-shaped, coherent γ' precipitates form with a $\{110\}_M/(010)_p$ habit plane. During conventional aging, all 6 variants of the $Ni_2(Mo,Cr)$ precipitates form and coarsen with aging time. With the application of external loading below the yield stress during aging, variants with $\{110\}_M$ habit planes that experience the largest dilations resulting from the externally applied stress are favored. Phase field modeling, coupled with elasticity theory, has been employed to simulate the development of variant selection of γ' precipitates with and without applied external loading. Similar to the experimental results, the γ' precipitates tend to form parallel to each other during coarsening and display variant selection when external stress is applied during aging. The mechanism is believed to be the reduction of elastic strain energy caused by the precipitate/matrix lattice mismatch. Thus, the nature of the selection indicates that the sign of the misfit is positive along $[010]_p$. Because the misfit strain energy increases with increasing precipitate size, variant selection occurs during coarsening.

1. Introduction

Ni base superalloys are widely used in high temperature environments, e.g., turbine engines, because of their excellent mechanical properties at elevated temperature, resistance to creep deformation and corrosion, and surface stability [1–3]. The most common strengthening mechanism for Ni base superalloys at high temperature is precipitation hardening caused by the formation of coherent $L1_2$ precipitates [4]. The cube-on-cube orientation relationship between the matrix and cubic precipitates results in only a single variant. However, the initially cuboidal precipitates are known to transform into lamellar "rafted" morphologies during high temperature creep, which significantly affects creep behavior [5]. Several studies of rafting of $L1_2$ precipitates have shown this phenomenon to be largely governed by the sign of applied stress, lattice misfit, and elastic moduli between the matrix and $L1_2$ precipitates, including anisotropic elastic effects [4–19]. Modeling based on elastic strains associated with the lattice misfit, as well as interfacial energies, has been successful in predicting rafting effects [1,19–22]. A competing plasticity model, based on edge components of slipping dislocations deposited on the matrix/precipitate interfaces during creep and their effect on lattice mismatch accommodation on interfaces parallel vs. perpendicular to the applied stress, also predicts rafting trends as a function of the sign of the mismatch and applied stress [14,23,24].

Variant selection has been investigated in other alloy systems, e.g., Ti [25–29], Al [30], Mg [31], and Fe alloy [32]. In the study by Eggeler [33,34], all Ni_4Ti_3 variants were formed in the interiors of grains while some variants were selected near grain boundaries when aging under stress [33]. In fact, they showed that, by aging a single crystal under stress, single variant Ni_4Ti_3 precipitates could be selected [34]. Most of the authors have attempted to explain variant selection in terms of precipitate interactions with defects, such as dislocations, grain boundaries, and twin boundaries [25,33], as well as effects of magnetic fields on variant selection in steels [32].

Given that the $Ni_2(Mo,Cr)$ γ' phase, of interest in this study, has the orthorhombic Pt_2Mo structure [35,36], the misfit between it

* Corresponding author.
** Corresponding author.
E-mail addresses: j.song.thu@gmail.com (J. Song), yao.fu@uc.edu (Y. Fu).

https://doi.org/10.1016/j.actamat.2018.11.063
1359-6454/

and the FCC matrix is expected to be anisotropic and variant selection might be expected to occur under the influence of external stress. A few studies have been conducted on variant selection of non-cubic precipitates during aging in Ni-based alloys [37]. For example, Oblak et al. aged single crystals of alloy 718 under an applied stress in an effort to promote/suppress certain variants of tetragonal DO_{22} phase. Based on the Oblak's study [37], phase field and ab-initio calculations were employed to investigate the effects of aging temperature, aging time, misfit, external stress, etc. on both the precipitate structure and the variant selection in IN718, which forms cubic $L1_2$ and tetragonal DO_{22} precipitates [1]. To the authors' knowledge, few experimental studies have systematically analyzed variant selection and morphology of the orthorhombic Ni_2(Mo,Cr) (i.e., Pt_2Mo type) phase during aging in Ni-based superalloys.

In the current study, single variants of Ni_2(Mo,Cr) precipitates were obtained by the application of loading below the yield stress during aging of Haynes 244 alloy [38,39]. The results have potential implications for the performance of this class of alloys. For example, different types/energies of faults result from dislocation cutting by different combinations of slip system and precipitate variants. Thus, anisotropic strengthening might be expected to result from variant selection within the grains. This phenomenon is the subject of ongoing work by the authors.

2. Experimental procedures

Haynes 244, a Ni-base low coefficient of thermal expansion (CTE) alloy, with the composition Ni-15.6Mo-10.2Cr-2.2W (at %), was employed in the current study. The samples were initially given a homogenization heat treatment at 1423 K for 24 h followed by 50% reduction by cold rolling and 1 h recrystallization at 1423 K. For the conventional aging process (no externally applied stress), the samples were aged in a resistance furnace under two conditions: 773 K for 4 h and 773 K for 4 h followed by 1023 K for 4 h. In addition, aging under 200 MPa applied stress (measured yield stress at this temperature was approximately 250 MPa) was conducted using a Gleeble 3500D instrument. Multiple aging times (0.25, 1, and 4 h) were employed to evaluate the effects of applied stress during aging on precipitate evolution.

Specimens were examined by scanning electron microscopy (SEM), electron backscatter diffraction (EBSD), and transmission electron microscopy (TEM). Samples for SEM and EBSD were prepared using standard metallographic procedures and were etched for 2 min with Kalling's No. 2 etchant. Samples for TEM analysis were prepared using a twin-jet polisher with a solution of 10 parts perchloric acid, 45 parts methanol, and 45 parts glacial acetic acid by volume, at 228 K and a potential of 15 V. In addition, site-specific TEM foils were produced by focused ion beam (FIB) on a FEI Helios instrument. The microstructures were examined using a JEOL 7000 field emission SEM (FE-SEM) equipped with EBSD, a Philips CM12 TEM, and a Talos F200X CTEM/STEM.

3. Simulation detail

Coupled phase field and elasticity theory is used to simulate the precipitate growth and morphology change with and without external elastic loading. In the phase field modeling, continuous variables that describe the microstructure vary smoothly over the interfaces from one phase to another. To account for the matrix and precipitates of different variants, a multiphase Kim-Kim-Suzuki (KKS) model [40,41] is employed with the order parameter η_1, η_2 representing the precipitates with eigenstrain in the $[110]_M$ and $[1\bar{1}0]_M$ directions of the matrix, respectively, and η_3 representing the matrix. It should be mentioned here that even though the precipitate has inherently six equivalent variants (eigenstrain directions), we simplify the situation in the computational model by considering two variants, with the applied loading favorable to the growth of one variant. Thus the nature of the problem remains the same yet the computational cost can be reduced, because a smaller simulation domain can be used with an adequate number of precipitates for each variant. The simulation is carried out in 2-D parallel to the (001) plane. The 2-D calculations can be considered equivalent to 3-D simulation with no change in concentration and microstructure along the third dimension. The material system is also simplified as a binary alloy of Ni and Mo, where the apparent composition of Mo is the summation of Mo and the other precipitate-forming element Cr. The variable c is used to represent the total concentration of Mo and Cr, and c_M and c_p denote its concentration in the matrix and precipitate phase, respectively.

Some of the notable features of the KKS model include: 1) large free energy penalty at the interface is remedied by introducing phase concentrations, i.e., the fractions of the total concentration held in a given phase, 2) the use of wide interface and coarser spatial discretization is allowed due to the decoupled interfacial energy from the diffuse interface width, 3) equality of the component chemical potentials across all phases is enforced, and 4) the formation of the spurious third phase at the binary interface between two phases is mitigated by requiring the switching functions to have the additional property of having zero slope and positive curvature perpendicular to the transformation path between two phases. Other details of the theoretical background of the multiphase KKS model can be found in Refs. [40,41].

The time evolution of the order parameters is dictated by the reduced free energy with time. More specifically, the evolution of non-conserved order parameters η_i is governed by the Allen-Cahn equation (Eqn. (1)), whereas the evolution of conserved order parameters c is governed by the Cahn-Hillard equation (Eqn. (2)).

$$\frac{\partial \eta_j}{\partial t} = -L_j \frac{\delta F}{\delta \eta_j},\ j = 1,\ 2,\ 3 \tag{1}$$

$$\frac{\partial c}{\partial t} = -\nabla \cdot \left(M_c \nabla \frac{\delta F}{\delta c} \right) \tag{2}$$

where L_j is the order parameter mobility, M_c the chemical mobility and F is the total free energy of the system [42], given by

$$F = \int_{\Omega} \left(f_{loc} + f_{gr} + E_{el} \right) dV \tag{3}$$

The local free energy f_{loc} is

$$f_{loc} = \sum_{i=1}^{3} \left[h_i f_i(c_i) + W \eta_i^2 (1 - \eta_i)^2 \right] \tag{4}$$

where f_i is the bulk free energy density of each phase, c_i is the phase concentration, W is the potential barrier height, and the h_i are the tilting functions given by

$$h_i = \frac{\eta_i^2}{4} \left(15(1 - \eta_i) \left[1 + \eta_i - \left(\eta_k - \eta_j \right) \right] + \eta_i \left(9\eta_i^2 - 5 \right) \right),\ i = 1, 2, 3 \tag{5}$$

where

$$j \equiv 1 + mod(i, 3)\ and\ k \equiv 1 + mod(i + 1, 3) \tag{6}$$

The gradient energy f_{gr} is

$$f_{gr} = \sum_{i=1}^{3} \frac{K}{2} |\nabla \eta_i|^2 \quad 7$$

where κ is the gradient energy coefficient.

The total concentration c is defined as a function of the phase concentrations c_i as

$$c = \sum_{i=1}^{3} h_i c_i \quad 8$$

The elastic energy E_{el} is

$$E_{el} = \sum_{i=1}^{3} \frac{1}{2} h_i \boldsymbol{\sigma}_i (\boldsymbol{\varepsilon}_i - \boldsymbol{\varepsilon}_i^*) \quad 9$$

where $\boldsymbol{\sigma}_i$, $\boldsymbol{\varepsilon}_i$, and $\boldsymbol{\varepsilon}_i^*$ are the stress, total strain, and eigenstrain in each phase i.

Eqn. (1) and Eqn. (2) are solved together with the mechanical equilibrium equation under no applied body force

$$\nabla \cdot \boldsymbol{\sigma} = 0 \quad 10$$

where $\boldsymbol{\sigma} = \sum_{i=1}^{3} h_i \boldsymbol{\sigma}_i$ following the Voight-Taylor scheme [43].

Following the procedure by Kim et al. [41], Eqn. (2) is equivalent to

$$\frac{\partial c}{\partial t} = -\nabla \cdot \left(D \sum_{i=1}^{3} h_i \nabla c_i \right) \quad 11$$

Eqn. (1), Eqn. (10), and Eqn. (11) are solved via the finite-element framework, open source Multiphysics Object-Oriented Simulation Environment (MOOSE), with the preconditioned Jacobian-free Newton Krylov (PJFNK) method.

4. Results

4.1. $Ni_2(Mo,Cr)$ crystallography structure

Based on the crystallographic relationship between the Pt_2Mo structure and FCC matrix shown in Fig. 1a [35,36], the lattice parameters of the $Ni_2(Mo,Cr)$ precipitates (γ') can be estimated from the matrix lattice parameter as $a_p = 1.5\sqrt{2}a_M$, $b_p = 0.5\sqrt{2}a_M$, and $c_p = a_M$, with the 6 possible correspondence variants (definition in Ref. [44]) listed in Table 1. Note that the actual lattice parameters for the precipitates will deviate slightly from these values, creating the lattice mismatch values that drive variant selection. The reflections expected in selected area diffraction patterns from Ni with the 6 different γ' variants are shown schematically in Fig. 1b for 7 major zone axes. In order to reveal all 6 γ' variants, diffraction data from at least three major zones must be collected. In this study, we used [112], [121], and [111] zone axes to reveal all 6 variants.

Centered dark field (CDF) TEM micrographs of γ' precipitates are shown in Fig. 2. The γ' precipitates are fully coherent with the Ni matrix and form in a lenticular-shaped morphology. The precipitates in contrast in Fig. 2a are being viewed normal to their habit plane (variant No. 2 in the indexing scheme of Fig. 1b and Table 1) and those in Fig. 2b are being viewed along a direction parallel to the habit plane (variant 4). The shape of the γ' precipitates indicates that the lattice misfit, which acts as a nucleation barrier for precipitation, is larger along the $[010]_p$/<110>$_M$ direction of the γ' phase compared with the orthogonal $[100]_p$ and $[001]_p$ directions.

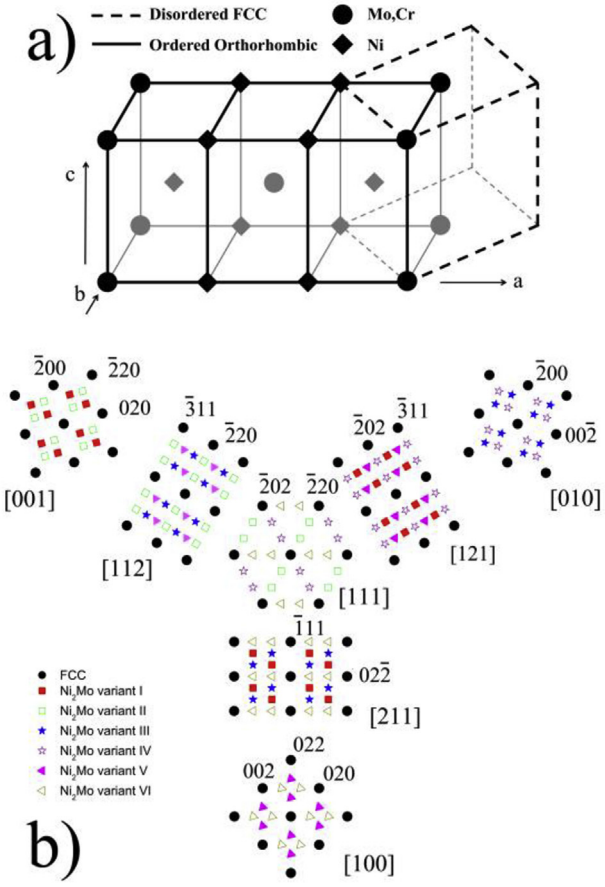

Fig. 1. a) Schematic of crystallographic relationship between Pt_2Mo structure and FCC matrix, and b) Schematic diffraction patterns from the FCC matrix containing the 6 γ' variants along different major zone axes according to the relationship listed in Table 1.

Table 1
6 Correspondence variants between γ' and the FCC matrix.

Variant	Relationship
I	$[100]_p \parallel [110]_M$; $[010]_p \parallel [\bar{1}10]_M$; $[001]_p \parallel [001]_M$
II	$[100]_p \parallel [1\bar{1}0]_M$; $[010]_p \parallel [110]_M$; $[001]_p \parallel [001]_M$
III	$[100]_p \parallel [101]_M$; $[010]_p \parallel [10\bar{1}]_M$; $[001]_p \parallel [010]_M$
IV	$[100]_p \parallel [\bar{1}01]_M$; $[010]_p \parallel [101]_M$; $[001]_p \parallel [010]_M$
V	$[100]_p \parallel [011]_M$; $[010]_p \parallel [0\bar{1}1]_M$; $[001]_p \parallel [100]_M$
VI	$[100]_p \parallel [01\bar{1}]_M$; $[010]_p \parallel [011]_M$; $[001]_p \parallel [100]_M$

4.2. Variant selection without external stress during aging

The microstructure of a specimen aged at 773 K for 4 h is shown in Fig. 3a–b. Fine intragranular precipitates can be seen as mottled contrast in the BF image (Fig. 3a) and the high resolution TEM (HREM) image shows the globular shape of the precipitates with ~5 nm diameter (Fig. 3a inset). Contributions from all 6 variants are present in the selected area diffraction (SAD) patterns (Fig. 3b). Images and diffraction data of the γ' precipitates after an additional 4 h aging at 1023 K (after the initial aging at 773 K for 4 h) are shown in Fig. 3c–d. The coarsened γ' precipitates are lenticular shaped (Fig. 3c). Again, contributions from all 6 variants are present in the SAD patterns. However, it is clear from the image and the diffraction patterns that the precipitate variants are clustered

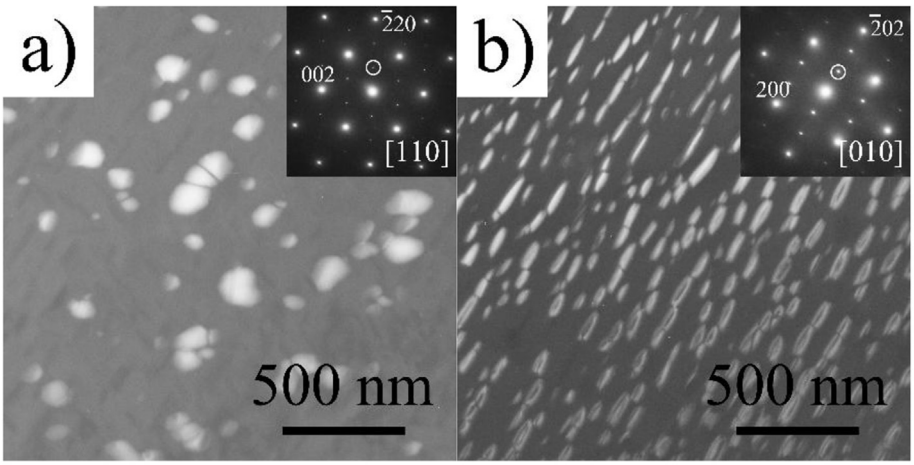

Fig. 2. CDF images with reflections indicated by circles on the micrographs. a) in [110] zone, and b) in [010] zone.

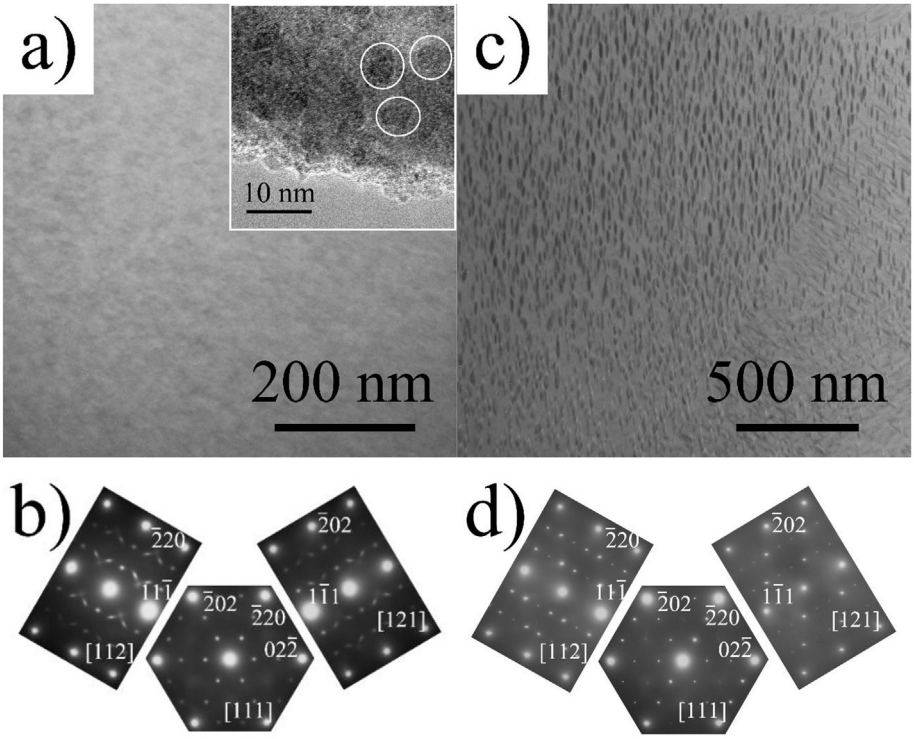

Fig. 3. BFTEM images (a, c) and SAD patterns (b, d) of 773 K/4 h/0 MPa sample and 773 K/4 h/0 MPa +1023 K/4 h/0 MPa sample, showing all 6 variants of γ′ precipitates. The inset in (a) is a HREM image taken down the [110] zone axis.

causing the reflections from the different variants to have different intensities in the diffraction patterns (Fig. 3d). In fact, it is clear that the γ′ precipitates of the same variant tend to cluster together into single variant pockets of γ′ in the microstructure. A mechanism explaining this phenomenon is presented in Chen's paper on the Ni-V-X alloy [31,45]. Different pockets contain different γ′ variants so that all 6 variants are observed in a large area.

4.3. Variant selection with uniaxial applied tensile stress during the aging process

SAD patterns from a sample aged for 4 h at 773 K under a 200 MPa applied stress are similar to those from the unstressed sample (Fig. 3b) and are shown in Fig. 4. All 6 variants can be seen in these patterns with similar intensity for all variant reflections, i.e., stress does not appear to affect variant selection of the γ′ precipitates in this condition. The structure of γ′ precipitates is also globular and similar to that seen in the sample aged with no externally applied stress, shown in Fig. 3a.

In the microstructures of samples subjected to an additional aging treatment of 1023 K for various aging times under a 200 MPa uniaxial stress, after initial aging at 773 K for 4 h with no applied stress, (Fig. 5-Fig. 7), the γ′ precipitates are large enough to be seen in the SEM and nearly all of the precipitates within individual grains appear to be parallel to each other (Fig. 5). The low magnification image in Fig. 5a shows the tensile direction and the FIB lift-out location for TEM analysis of Grain 1. The $\{110\}_M$ plane traces obtained from EBSD analysis are overlaid on these images by the

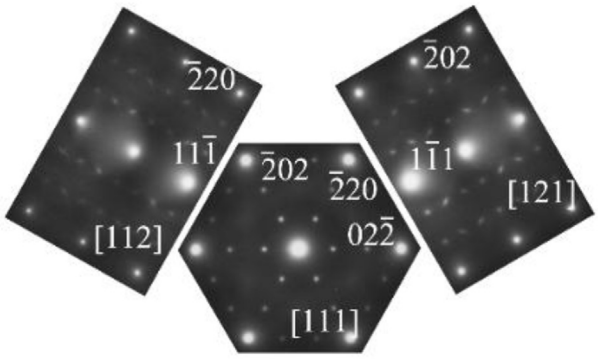

Fig. 4. SAD patterns from the sample aged at 773 K/4 h/200 MPa, showing contributions from all 6 variants of the γ′ precipitates.

method described in Appendix A. Detailed orientation information is displayed in Table 2. Under load, the six planes in the $\{110\}_M$ family have different dilations due to different orientations with respect to the applied stress; these can be determined by the procedure provided in Appendix B and the values for the different grains analyzed are shown in Table 2. The last row in Table 2 shows the dilations that would be produced for the 6 different $\{110\}_M$ planes by a tensile strain along the $[110]_M$ direction, for reference. In the interior of grain 1, most of the γ′ precipitates are parallel to the $(011)_M$ plane trace (Fig. 5b) and this plane has the highest dilation (0.762×10^{-3}) associated with the applied stress (Table 2). Grain 2 yielded similar results, with the dominant $(1\bar{1}0)_M$ variant plane having the maximum dilation (0.708×10^{-3}), as shown in Fig. 5c. In grain 3, two variants of γ′ precipitates can be seen, with the dominant one parallel to the $(1\bar{1}0)_M$ plane trace and the other parallel to the $(10\bar{1})_M$ plane trace (Fig. 5d). According to the calculations in Table 2, the dominant variant has the maximum dilation of the habit plane (0.639×10^{-3}) and the other one has the second highest dilation (0.468×10^{-3}). It is worth mentioning that the habit planes that have the highest dilations are found under the uniaxial stress state assumption of individual grain. In a polycrystalline structure of anisotropic materials such as nickel, the stress state of each grain could deviate from the external loading

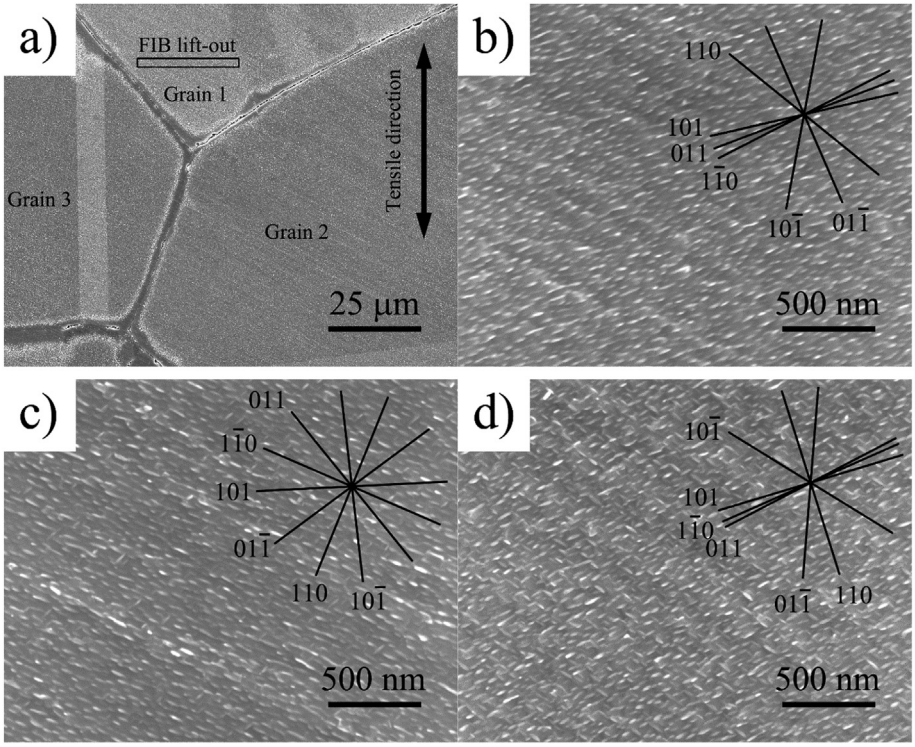

Fig. 5. SEM images of 773 K/4 h/0 MPa + 1023 K/4 h/200 MPa sample. a) low magnification image shows the tensile direction and FIB lift-out location, b) Grain 1 with $\{110\}_M$ plane traces, c) Grain 2 with $\{110\}_M$ plane traces, and d) Grain 3 with $\{110\}_M$ plane traces.

Table 2
The tensile directions and metallographic sample plane normals (obtained by EBSD) and elastic strain values along the six $<110>_M$ directions during aging under a 200 MPa load. The last row shows dilations for the 6 $\{110\}_M$ planes for a 200 MPa tensile load along the $[110]_M$ direction for reference.

773 K/4 h/0 MPa +1023 K/200 MPa	Tensile direction: [uvw] Plane normal: (hkl)	Strain (1×10^{-3})					
		$1\bar{1}0$	110	$10\bar{1}$	101	$01\bar{1}$	011
4 h (Grain 1)	[2 11 6] (19 $\bar{1}0$ 12)	0.124	0.343	−0.357	−0.238	0.106	0.762
4 h (Grain 2)	[$\bar{9}$ 15 $\bar{6}$] ($\bar{2}1$ $\bar{1}9$ $\bar{2}3$)	0.708	0.071	−0.353	−0.154	0.410	0.057
4 h (Grain 3)	[$\bar{7}$ 4 3] ($\bar{6}$ $\bar{3}$ $\bar{1}0$)	0.639	0.034	0.468	0.014	−0.338	−0.078
1 h (Grain 1)	[5 7 9] (0 $\bar{9}$ 7)	−0.248	0.113	−0.092	0.373	−0.029	0.622
0.25 h	[26 10 19] (2 $\bar{9}$ 2)	−0.044	0.322	0.023	0.718	−0.274	−0.006
Ref. 200 MPa	[110]	0.059	0.859	−0.045	−0.045	−0.045	−0.045

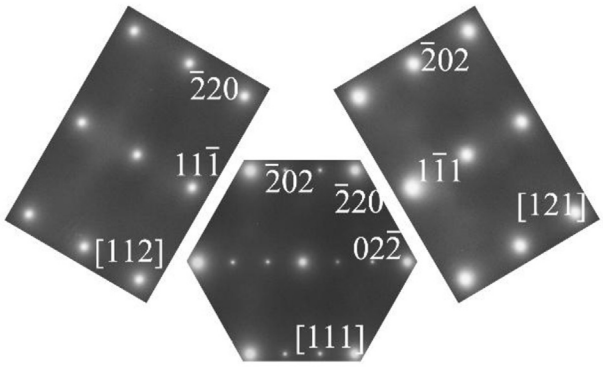

Fig. 6. SAD patterns from 773 K/4 h/0 MPa + 1023 K/4 h/200 MPa sample from the FIB lift-out shown in Fig. 5a.

condition. The planes that have the largest normal strains, however, remain the same when the stress states in the individual grain deviate from the uniaxial loading condition due to the polycrystalline structure, as demonstrated in the Appendix B.

The cross-section of the FIB lift-out for Grain 1 was chosen to be perpendicular to the tensile direction, i.e., the beam direction at zero tilt is approximately parallel to the tensile direction. The angles between the major zones ([112], [211], and [121] zone axes) and the beam direction at zero tilt were also used to calculate the tensile direction along the FIB lift-out foil normal. The resulting direction is within 5° of that determined by EBSD (see Appendix C). The SAD patterns (Fig. 6) from the FIB lift-out (Fig. 5a) confirm the presence of a single variant (No. 6) in this region with the $[010]_p$ direction of the γ′ lenticular precipitates perpendicular to the $(011)_M$ plane (Fig. 1b and Table 1). This is consistent with the results of the plane trace from EBSD data shown in Fig. 5b. Thus, it can be concluded that the γ′ precipitates tend to develop on the $\{110\}_M$ habit planes with the maximum dilations caused by the externally applied stress.

The microstructure of a sample aged under stress for an additional 1 h at 1023 K following the 773 K/4 h stress-free aging treatment is shown in Fig. 7a. At higher magnification (Fig. 7b), the orientations of the γ′ precipitates in Grain 1 are parallel to each other, with habit planes consistent with either $(011)_M$ or $(01\bar{1})_M$ plane traces. SAD patterns (Fig. 7c) from a FIB lift-out specimen, shown in Fig. 7a, confirm that only one variant of γ′ precipitates formed in this region. This variant is No. 6 (Table 1 and Fig. 1b), with a habit plane parallel to the maximally dilated $(011)_M$ as seen in Table 2.

The microstructure of the sample given an additional 0.25 h aging at 1023 K under the 200 MPa applied stress following the 773 K/4 h stress-free aging treatment contains slightly larger γ′ precipitates and a reduced number of variants as indicated by the SAD patterns taken from the FIB lift-out (Fig. 7d), i.e. variants of γ′ precipitates have been selected by the applied stress during aging. The orientation and related elastic strains for the $\{110\}_M$ planes of the FIB lift-out region are listed in Table 2. Again, the γ′ precipitates tend to form on the $\{110\}_M$ planes with the largest elastic dilations due to the applied stress; in this case, these are variants 2 and 4, which exhibit the strong reflections and experience the highest dilations, and a small amount of variant 5.

4.4. Phase field modeling with/without external applied stress during aging

Experimental results using samples aged under applied stress show that single variants tend to form on the $\{110\}_M$ habit planes

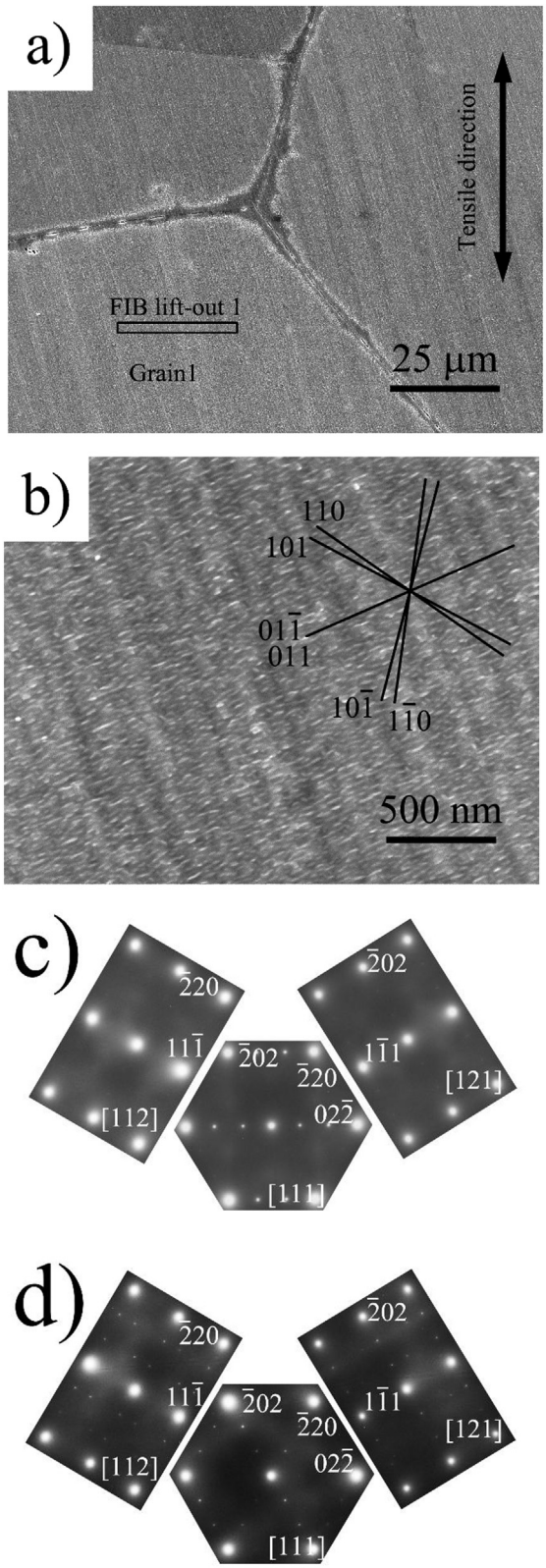

Fig. 7. SEM images and SAD patterns from the 773 K/4 h/0 MPa + 1023 K/1 h/200 MPa sample. a) low magnification image shows the tensile direction and FIB lift-out location, b) Grain 1 with $\{110\}_M$ plane traces indicated, c) SAD patterns from the FIB lift-out showing a single variant of γ′ precipitates, and d) SAD patterns from the FIB lift-out showing reflections from 3 variants of the γ′ precipitates in the 773 K/4 h/0 MPa + 1023 K/0.25 h/200 MPa sample.

with the maximum dilations/normal strains. The lenticular-shape of the precipitates indicates that the misfit strain is small within the habit plane but large normal to it. It is expected that dilatation from external loading can thus alleviate the misfit strain of favorably oriented variants during growth, resulting in variant selection. A phase field simulation is employed to demonstrate feasibility for this mechanism. The simulation results can be considered to correspond to an area within the grain, where one dominant variant experiences the maximum dilation of its habit plane resulting from the external loading, for example, the interior of grain 1 or 2 in Fig. 5. Similar simulation approaches have been used in Refs. [1,46].

A domain size of 300 nm × 300 nm is considered with an initial grid size of around 2 nm and adaptive mesh algorithm to refine the mesh at the interfaces. Periodic boundary condition is applied to all boundaries. The materials parameters necessary for the simulation are estimated based on either experimental results or relevant first-principles based simulations. The interface energy σ is chosen as 30 mJ/m^2 considering the coherent interface between matrix and precipitate. Interface thickness l is estimated to be around 2 nm. The diffusion coefficient of the solution (Mo and Cr element) D is on the order of 10^{-12} mm^2/s, estimated based on experimental diffusion studies of Cr and Mo in Ni based alloys in the 900 K–1100 K range [47–49]. The equilibrium chemical concentrations of Mo in the matrix and precipitate are 0.2 and 0.33, respectively. Thus the free energies of the precipitate $f_p(c_p)$ and matrix $f_M(c_M)$ are approximated with parabolic free energies, $f_p(c_p) = V_m^{-1} C_p (c_p - c_{pe})^2$ and $f_p(c_p) = V_m^{-1} C_M (c_M - c_{Me})^2$ with minima at $c_{pe} = 0.33$ and $c_{Me} = 0.2$. The coefficients C_p and C_M are estimated as $5.7 \times 10^5\ J/mol$ and $1.9 \times 10^5\ J/mol$, respectively, and the molar volume is approximately $2.4 \times 10^{-5}\ m^3/mol$. The parameters for the physical model can be derived from these materials parameters. The gradient energy coefficient κ and potential barrier height W can be calculated from the interface energy and thickness as $\kappa = 3\sigma l = 1.8 \times 10^{-10}\ J/m$ and $W = 6\sigma/l = 9.0 \times 10^7\ J/m^3$. The change in the largest semi-principal axes r of the precipitates with time t is observed in TEM and fitted to $r = \alpha_\lambda (Dt)^{0.5}$, where α_λ is the growth coefficient that relates to the supersaturation and D is the diffusion coefficient [50]. Thus, using interface velocity $V = dr/dt = 0.5\alpha_\lambda^2 D/r = L\kappa/r$, the mobility of order parameter is estimated as $L = 0.5\alpha_\lambda^2 D/\kappa = 1.9 \times 10^{-9} m^3/(Ns)$ based on Allen and Cahn's description for a diffuse-interface [51,52]. Finally, the stiffness matrix $\mathbf{C}$ of the precipitate is obtained from the Vegard's law and first-principles based calculation of Ni_2Mo and Ni_2Cr [53], and that of the matrix is approximated by pure nickel [54]. The stiffness matrix can be transformed given the crystal direction of the coordinate system by following the procedure given in the Appendix B.

As mentioned previously, two variants are chosen for the precipitates, each with an initial value of $\eta_i(average) = 0.15$ and a random fluctuation in the magnitude of $\Delta\eta_i = \pm 0.0625$ to introduce homogeneous nuclei of both variants. The initial concentration field c also has a fluctuation of ±0.0625 around the average 0.25, so the matrix is saturated with the Mo/Cr elements. The x-axis of the simulation domain is aligned with the $[110]_M$ crystal direction of the matrix and the y-axis aligned with $[1\bar{1}0]_M$ direction. The left and bottom boundary are kept at zero x and y displacement throughout the simulation, respectively. The eigenstrains (or stress-free transformation strain) of the precipitates in the current coordinate system are nonzero along the x and y directions, respectively, based on the related studies for coherent precipitates in nickel-based superalloys [1,11,45,53,55],

$$\varepsilon^{\eta 1} = \begin{bmatrix} 0.5\% & 0 \\ 0 & 0 \end{bmatrix} \quad (12)$$

$$\varepsilon^{\eta 2} = \begin{bmatrix} 0 & 0 \\ 0 & 0.5\% \end{bmatrix} \quad (13)$$

With the loading applied along the x axis, the η_1 variant is found to have a larger dilatation of its habit plane compared to the η_2.

Under no external elastic loading, the growth of precipitates of both variants can be observed driven by the reduced chemical free energy, accompanied by the coalesce of adjacent grains of the same variant (Fig. 8). As expected and similar to experimental observations, precipitates demonstrate a lenticular shape and elongate perpendicular to the direction of the large misfit to reduce the elastic energy (Fig. 8). This demonstrates a dominance of elastic energy over interfacial energy thus favoring a large aspect ratio to reduce the elastic energy. Therefore, the precipitates of two different variants (i.e., $[110]_M$ and $[1\bar{1}0]_M$) are perpendicular to each other. The shrinkage of small precipitates and coarsening of large precipitates is also noticeable as early as around 1000 s.

In contrast, the precipitates with misfit in the x direction dominate after an applied stress of 200 MPa along the x axis (the upper boundary in the y direction is kept stress-free). Those precipitates with a large misfit in the y direction failed to either nucleate or grow during the aging process (Fig. 9). The large aspect ratio of the precipitates at later stages is partially caused by the coalesce of adjacent precipitates having the same variant, which causes some quantitative discrepancies from the experimental results. Despite the simplification of the computational model and approximations of some materials parameters, these simulations demonstrate that the precipitate variant can be selected by the externally applied loading.

5. Discussion

The intragranular $Ni_2(Mo,Cr)$ precipitates (γ') in the current study are fully coherent with the matrix. Their morphology is lenticular, with the broad faces parallel to the $\{110\}_M$ habit planes of the matrix and the $(010)_p$ plane of γ' structure (Table 1 and Fig. 2). From this observation, it is likely that the misfit strain (misfit energy, ΔG_s) of the lenticular-shaped precipitates is small within the habit plane and large in the direction normal to the habit plane, i.e., along $[010]_p$. The activation barrier for nucleation (ΔG^*) and elastic energy increase during coarsening due to elastic strain can therefore be assumed to be mainly derived from the misfit strain in the $[010]_p$ direction, as given by Eqn. (14).

$$\Delta G_s \approx d\delta^2 V \quad (14)$$

where d is a constant determined by the shear modulus and composition of the matrix, V is the precipitate volume, and δ is the misfit.[1] As discussed in a previous paper [56–58], the presence of vacancies significantly reduces the misfit strain energy, ΔG_s, thus lowering the nucleation barrier. At the nucleation stage, the misfit, δ, can be reduced in all directions by the presence of vacancies. The globular shape of the γ' precipitates during the early aging supports this argument (Fig. 3a). Also, the elastic strain energy should be less dominant compared with the interfacial energy when the precipitate volume is small, i.e. during nucleation and early growth. Thus, a globular shape, which has the lowest interface area to volume ratio, is favored.

[1] Misfit is calculated by $(a_p\text{-}a_M)/a_M$.

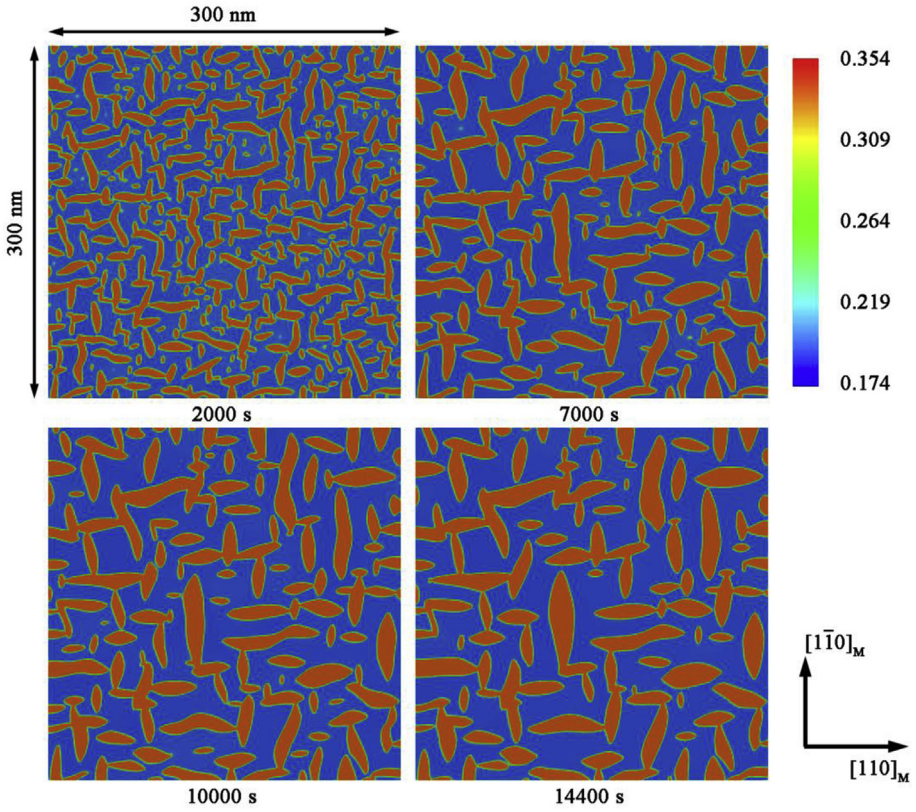

Fig. 8. Evolution of the precipitate morphology (represented by concentration field) with time without external loading.

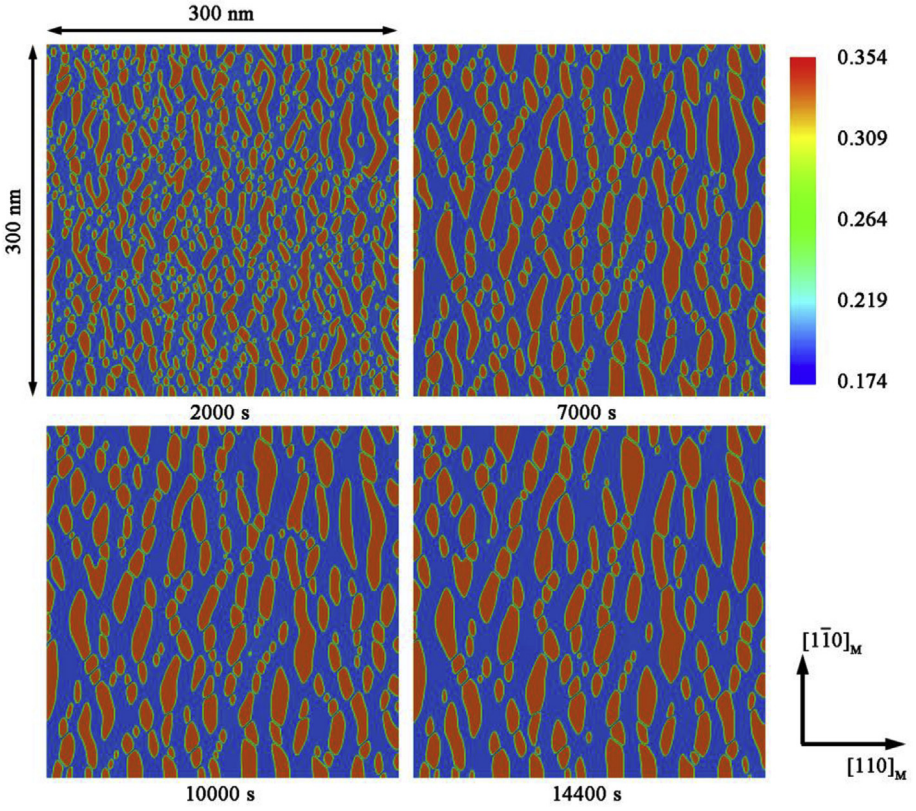

Fig. 9. Evolution of the precipitate morphology (represented by concentration field) with time under an applied stress of 200 MPa in the horizontal direction.

When a uniaxial external loading below the yield stress is applied during the aging process, the elastic strains will vary for the different habit plane normals according to the calculations in Appendix B. However, given that these differences are relatively small, as shown in Table 2, the effect on γ′ nucleation is small relative to the effect of quenched-in vacancies. For this reason, there is no variant selection of γ′ precipitates in the early stages of nucleation and growth as shown in Figs. 3 and 4. In addition, at the early stage of aging, the precipitates are globular shape either with or without external applied stress, more evidence that the effect of misfit anisotropy can be neglected during nucleation and early growth. Thus, in the early stages of nucleation and growth, all 6 variants are equally represented regardless of the applied stress (e.g., Fig. 4).

The results from the two-step aging under no external stress show localized pockets of single variant γ′ precipitates in the grain interiors (Fig. 3c–d), i.e., the γ′ precipitates tend to form parallel to each other within localized regions. This phenomenon occurs during coarsening of the γ′ precipitates after additional aging at 1023 K, following the initial 773 K age [45]. In contrast, upon aging at 1023 K under an externally-applied uniaxial stress, the entire grain exhibits a reduced number of variants, even though the γ′ precipitates were distributed randomly after initially aging at 773 K with no stress (Figs. 5–9).

During γ′ coarsening, the misfit strain energy, ΔG_s, increases with increasing precipitate volume according to Eqn. (14). In addition, the quenched-in vacancies are not stable at the aging temperature. If these vacancies do not bond with embryos during the early nucleation stage, they will diffuse to and annihilate at the grain boundaries. Therefore, the dilatational strains caused by the external stress for different $<110>_M/[010]_p$ directions reduces the misfit strain energy for the γ′ precipitating on these different {110} the $_M$ habit planes. Consequently, the γ′ precipitates tend to grow more quickly and align themselves parallel to each other in order to minimize ΔG_s. From the results shown in Figs. 5–9 and Table 2, the γ′ precipitates tend to form on the $\{110\}_M$ habit planes with the highest dilations.

6. Conclusions

Variant selection of intragranular, coherent $Ni_2(Mo,Cr)$ precipitates (γ′) can be controlled by applying an applied loading below the yield stress during coarsening (aging). At the early stage of aging, the shape of γ′ precipitates is globular, because the misfit strain energy is small at this stage. However, these γ′ precipitates are lenticular shaped with $\{110\}_M$ habit planes during coarsening (aging). The misfit is not uniform and appears to be higher along $[010]_p$. The misfit in the $[010]_p$ direction is positive. During nucleation and early growth, excess vacancies can alleviate the misfit strain and all 6 equivalent variants are formed in the matrix with or without the application of an external stress. However, a reduction in the number of variants is achieved during coarsening by applying an external stress. As the size of the γ′ precipitates reaches ~100 nm in lenticular diameter, single variant γ′ regions can be observed where the precipitates lie parallel to the habit planes with maximum dilations caused by the externally-applied stress. Because the misfit strain energy increases with size, the precipitation is initially uniform and multi-variant but, during coarsening, the increased strain energy leads to variant selection as a means of reducing the strain energy of the system. This results in only one or two variants becoming dominant during coarsening under stress. It is expected that this finding can benefit applications in many areas related to Ni-based superalloys.

Acknowledgements

We are grateful to Haynes International Inc. for supplying these alloys. In addition, the authors want to acknowledge support of the NSF I/UCRC Center for Advanced Non-Ferrous Structural Alloys and the member companies as well as the use of the instruments in the Electron Microscopy Laboratory at the Colorado School of Mines. The authors also want to acknowledge support of the Ohio Supercomputer Center.

Appendix

A. {110} plane traces determined by EBSD (FCC structure)

From the orientation of grain/sample determined by EBSD, i.e., the crystal direction of a grain in the *x*, *y*, *z* sample direction, the $\{110\}_c$ plane traces can be determined by following procedures and drawn over the images in Figs. 5–7. Here subscript *s* denotes the sample coordinates, and *c* denotes the crystal coordinates. The information retrieved from EBSD analysis can be expressed as

$$[100]_s//[v_{11}v_{12}v_{13}]_c, [010]_s//[v_{21}v_{22}v_{23}]_c, [001]_s//[v_{31}v_{32}v_{33}]_c$$

where the v_{ij} are the crystal indices. The plane normals of $\{110\}_c$ in the sample coordinates can be computed by the angle between $\{110\}_c$ and the corresponding axis unit vector. Take the $(110)_c$ as an example,

$$\cos\alpha = \frac{[110]\cdot[v_{11}v_{12}v_{13}]}{\|110\|\|v_{11}v_{12}v_{13}\|} \quad \cos\beta = \frac{[110]\cdot[v_{21}v_{22}v_{23}]}{\|110\|\|v_{21}v_{22}v_{23}\|} \quad \cos\gamma = \frac{[110]\cdot[v_{31}v_{32}v_{33}]}{\|110\|\|v_{31}v_{32}v_{33}\|}$$

where α, β, γ are the angle between $(110)_c$ and the x, y, z sample axis. So $(110)_c$ can be represented in the sample coordinates by the plane normal as $\boldsymbol{N}_s^{(110)_c} = \frac{[\cos\alpha\ \cos\beta\ \cos\gamma]}{\|\cos\alpha\ \cos\beta\ \cos\gamma\|}$. Further one can obtain the $\{110\}_c$ plane traces by the intersection between the {110}c plane and the $(001)_s$ x-y plane represented by $\boldsymbol{N}_s^{(001)_s}$ through $\boldsymbol{N}_s^{\{110\}_c} \times \boldsymbol{N}_s^{(001)_s}$.

B. $\{110\}_c$ plane dilation calculation (FCC structure)

The dilation in $\{110\}_c$ plane can be estimated by the elastic constants of nickel, C_{ijkl}, and the constitutive equation of anisotropic materials in the form of $\sigma_{ij} = C_{ijkl}\varepsilon_{kl}$ or $\varepsilon_{ij} = S_{ijkl}\sigma_{kl}$. Here σ_{ij} are components of stress, $\varepsilon_{ij} = (u_{i,j} + u_{j,i})/2$ are the components of the infinitesimal strain tensor, C_{ijkl} and S_{ijkl} is the elasticity and compliance tensor, respectively.

The elastic constant matrix in the coordinate system $\{\mathbf{e}_1, \mathbf{e}_2, \mathbf{e}_3\}_c$ with the crystal coordinate system parallel to the sample coordinate system (i.e., $\mathbf{e}_1 = [100]$, $\mathbf{e}_2 = [010]$, $\mathbf{e}_3 = [001]$) is given by $\mathbf{C}^{(\mathbf{e})}$,

$$\mathbf{C}^{(\mathbf{e})} = \begin{bmatrix} C_{11} & C_{12} & C_{12} & & & \\ C_{12} & C_{11} & C_{12} & & & \\ C_{12} & C_{12} & C_{11} & & & \\ & & & C_{44} & & \\ & & & & C_{44} & \\ & & & & & C_{44} \end{bmatrix}$$

where C_{11}, C_{12}, and C_{44} are three independent elastic constants, and have the values of 247 GPa, 147 GPa, and 125 GPa for nickel at 300 K [59]. Thus the elastic constant matrix in the coordinate system with crystal direction $\{\mathbf{m}_1, \mathbf{m}_2, \mathbf{m}_3\}_c$ parallel to the sample *x*, *y*, *z* axis ($\mathbf{m}_1$,

$\mathbf{m}_2$, $\mathbf{m}_3$ given by EBSD analysis) can be obtained by $\mathbf{C}^{(\mathbf{m})} = \mathbf{K}\mathbf{C}^{(\mathbf{e})}\mathbf{K}^T$, where the rotation matrix $\mathbf{K}$ is computed from the transformation tensor $\mathbf{\Omega}_{(\mathbf{m})}$ [60],

$$\left[\mathbf{\Omega}_{(\mathbf{m})}\right] = \begin{bmatrix} \mathbf{m}_1\cdot\mathbf{e}_1 & \mathbf{m}_1\cdot\mathbf{e}_2 & \mathbf{m}_1\cdot\mathbf{e}_3 \\ \mathbf{m}_2\cdot\mathbf{e}_1 & \mathbf{m}_2\cdot\mathbf{e}_2 & \mathbf{m}_2\cdot\mathbf{e}_3 \\ \mathbf{m}_3\cdot\mathbf{e}_1 & \mathbf{m}_3\cdot\mathbf{e}_2 & \mathbf{m}_3\cdot\mathbf{e}_3 \end{bmatrix}$$

So the elastic strain in the sample coordinates can be calculated by $\boldsymbol{\sigma}^{(\mathbf{m})} = \mathbf{C}^{(\mathbf{m})}\boldsymbol{\varepsilon}^{(\mathbf{m})}$. The dilation (elastic strain) in the crystal directions of interest, i.e., in $\{110\}_c$ plane normal directions, can be computed from $\boldsymbol{\varepsilon}^{(\mathbf{m})}$ by $\boldsymbol{\varepsilon}^{(\mathbf{q})} = \mathbf{\Omega}_{(\mathbf{q})}\boldsymbol{\varepsilon}^{(\mathbf{m})}\mathbf{\Omega}^T_{(\mathbf{q})}$, where $\mathbf{q} = \{\mathbf{q}_1, \mathbf{q}_2, \mathbf{q}_3\}$ is formed by the crystal directions and $\mathbf{\Omega}_{(\mathbf{q})ij} = \mathbf{q}_i\cdot\mathbf{m}_j$.

The above elastic strain calculation is based on uniaxial stress state condition. Since a polycrystalline sample is studied, the stress field in each individual grain could deviate from the uniaxial stress state. A 2D model that consists of 36 randomly-oriented nickel grains are constructed to evaluate the effect of stress variation on the calculated dilation. The elastic matrix given in ref. [54] is employed. A uniaxial loading of 200 MPa is applied along the horizontal direction (x direction).

The calculated stress states are shown in Fig. A1 and the stress variation among the grains can be observed. The maximum stress deviation is mainly found at the grain and domain boundaries.

The stress states in the grain interiors in all grains (except those at domain boundaries) are investigated and the two grains circled in white are found to have the largest stress variation from the uniaxial stress state given by:

$$\boldsymbol{\sigma}_1 = \begin{bmatrix} 250 & -30 & 0 \\ -30 & 25 & 0 \\ 0 & 0 & 0 \end{bmatrix} \text{MPa and } \boldsymbol{\sigma}_2 = \begin{bmatrix} 150 & 10 & 0 \\ 10 & -25 & 0 \\ 0 & 0 & 0 \end{bmatrix} \text{MPa}$$

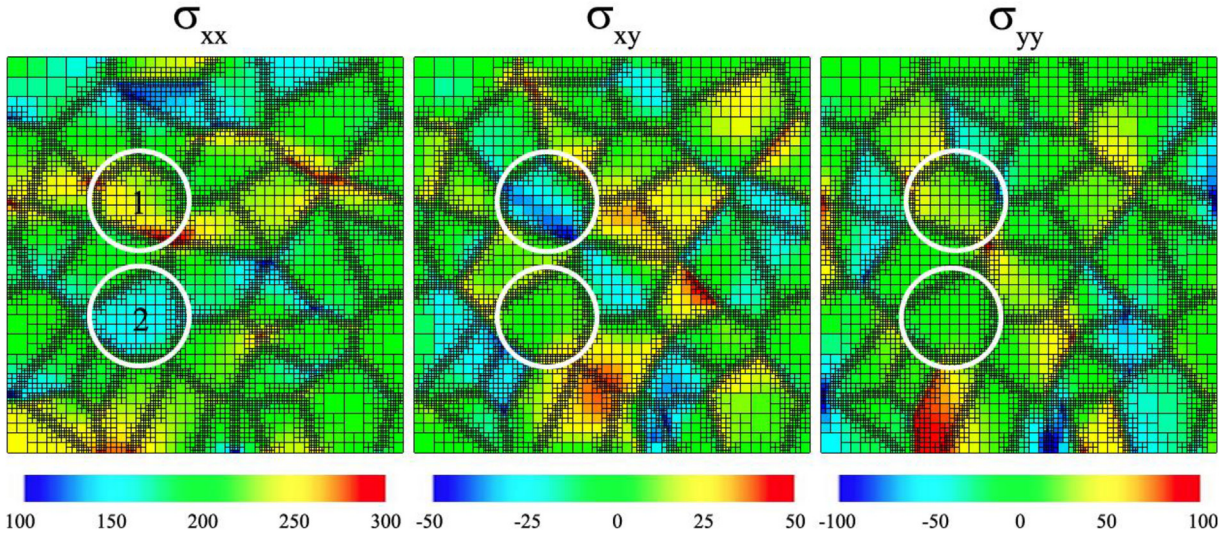

Fig. A1. Stress analysis of the polycrystalline structure of nickel under uniaxial loading of 200 MPa along the horizontal direction (x direction).

The normal strains on the six $\{110\}_c$ habit planes based on these stress states are computed and are given in the table below. Even though the strain values have changed, the planes that have the largest normal strains remain the same when compared with those calculated under uniaxial stress state. Further, the order of the strain components in terms of their values barely changes. Please note these are the extreme conditions; other grains with less deviation should have limited changes in the calculated strain value. This simple check using a 2D model supports the approach of explaining variant selection by resolving the stresses and calculating the normal strains in each grain based on the externally applied load.

Table A1
Normal strain computed on the six $\{110\}_M$ habit planes under different stress states (773 K/4 h/0 MPa + 1023 K/4 h/200 MPa): Grain 1 with [2 11 6] tensile direction and (19 $\overline{10}$ 12) plane normal; Grain 2 with [$\overline{9}$ 15 $\overline{6}$] tensile direction and ($\overline{21}$ $\overline{19}$ $\overline{23}$) plane normal.

	Stress state $\sigma = [\sigma_{xx}\sigma_{yy}\sigma_{zz}\sigma_{xy}\sigma_{xz}\sigma_{yz}]$	Strain (1×10^{-3})					
		$1\bar{1}0$	110	$10\bar{1}$	101	$01\bar{1}$	011
Grain 1	uniaxial: [200 0 0 0 0 0]	0.124	0.343	−0.357	−0.238	0.106	0.762
	$\boldsymbol{\sigma}_1$: [250 25 0−30 0 0]	0.162	0.610	−0.451	−0.350	0.194	0.852
	$\boldsymbol{\sigma}_2$: [150−25 0 10 0 0]	0.110	0.192	−0.328	−0.162	0.038	0.612
Grain 2	uniaxial: [200 0 0 0 0 0]	0.708	0.071	−0.353	−0.154	0.410	0.057
	$\boldsymbol{\sigma}_1$: [250 25 0−30 0 0]	0.965	0.089	−0.305	−0.176	0.397	0.050
	σ_2: [150−25 0 10 0 0]	0.488	0.053	−0.394	−0.130	0.385	0.060

C. Direction determination of FIB lift out (foil normal)

The crystal indices in the beam direction, [h k l], can be simply obtained by the angles α, β, and γ between [112], [211], or [121] and zero tilt direction (foil normal) from TEM analysis:

$$\begin{bmatrix} h \\ k \\ l \end{bmatrix} = \begin{bmatrix} 1 & 1 & 2 \\ 2 & 1 & 1 \\ 1 & 2 & 1 \end{bmatrix}^{-1} \begin{bmatrix} \cos\alpha \\ \cos\beta \\ \cos\gamma \end{bmatrix}$$

References

[1] N. Zhou, D.C. Lv, H.L. Zhang, D. McAllister, F. Zhang, M.J. Mills, Y. Wang, Computer simulation of phase transformation and plastic deformation in IN718 superalloy: microstructural evolution during precipitation, Acta Mater. 65 (2014) 270–286.

[2] G.A. Webster, B.J. Piearcey, An interpretation of the effects of stress and temperature on the creep properties of a nickel-base superalloy, Met. Sci. 1 (1) (1967) 97–104.

[3] M. Sundararaman, P. Mukhopadhyay, S. Banerjee, Some aspects of the precipitation of metastable intermetallic phases in inconel-718, Metall Trans A 23 (7) (1992) 2015–2028.

[4] A.J. Ardell, R.B. Nicholson, On the modulated structure of aged Ni-Al alloys: with an Appendix on the elastic interaction between inclusions by J. D. Eshelby, Acta Metall. 14 (10) (1966) 1295–1309.

[5] M. Kamaraj, Rafting in single crystal nickel-base superalloys - an overview, Sadhana Acad. Proc. Eng. Sci. 28 (1) (2003) 115–128.

[6] J.C. Chang, S.M. Allen, Elastic energy changes accompanying gamma-prime rafting in nickel-base superalloys, J. Mater. Res. 6 (09) (1991) 1843–1855.

[7] M. Doi, Elasticity effects on the microstructure of alloys containing coherent precipitates, Prog. Mater. Sci. 40 (2) (1996) 79–180.

[8] W.C. Johnson, Precipitate shape evolution under applied stress - thermodynamics and kinetics, Metall Trans A 18 (2) (1987) 233–247.

[9] W.C. Johnson, M.B. Berkenpas, D.E. Laughlin, Precipitate shape transitions during coarsening under uniaxial stress, Acta Metall. 36 (12) (1988) 3149–3162.

[10] C.A. Laberge, P. Fratzl, J.L. Lebowitz, Microscopic model for directional coarsening of precipitates in alloys under external load, Acta Mater. 45 (10) (1997) 3949–3962.

[11] D.Y. Li, L.Q. Chen, Computer simulation of morphological evolution and rafting of γ' particles in Ni-based superalloys under applied stresses, Scripta Mater. 37 (9) (1997) 1271–1277.

[12] D.Y. Li, L.Q. Chen, Shape evolution and splitting of coherent particles under applied stresses, Acta Mater. 47 (1) (1998) 247–257.

[13] A. Pineau, Influence of uniaxial stress on the morphology of coherent precipitates during coarsening—elastic energy considerations, Acta Metall. 24 (6) (1976) 559–564.

[14] T.M. Pollock, A.S. Argon, Directional coarsening in nickel-base single crystals with high volume fractions of coherent precipitates, Acta Metall. 42 (6) (1994) 1859–1874.

[15] I. Schmidt, D. Gross, Directional coarsening in Ni–base superalloys: analytical results for an elasticity–based model, Proc. Roy. Soc. Lond.: Math. Phys. Eng. Sci. 455 (1988) 3085–3106, 1999.

[16] J.K. Tien, S.M. Copley, The effect of uniaxial stress on the periodic morphology of coherent gamma prime precipitates in nickel-base superalloy crystals, Metall. Trans. 2 (1) (1971) 215–219.

[17] M. Véron, P. Bastie, Strain induced directional coarsening in nickel based superalloys: investigation on kinetics using the small angle neutron scattering (SANS) technique, Acta Mater. 45 (8) (1997) 3277–3282.

[18] M. Véron, Y. Bréchet, F. Louchet, Strain induced directional coarsening in Ni based superalloys, Scripta Mater. 34 (12) (1996) 1883–1886.

[19] N. Zhou, C. Shen, M.J. Mills, Y. Wang, Contributions from elastic inhomogeneity and from plasticity to γ' rafting in single-crystal Ni–Al, Acta Mater. 56 (20) (2008) 6156–6173.

[20] P. Fratzl, O. Penrose, J.L. Lebowitz, Modeling of phase separation in alloys with coherent elastic misfit, J. Stat. Phys. 95 (5) (1999) 1429–1503.

[21] M.P. Gururajan, T.A. Abinandanan, Phase field study of precipitate rafting under a uniaxial stress, Acta Mater. 55 (15) (2007) 5015–5026.

[22] R. Mukherjee, T.A. Abinandanan, M.P. Gururajan, Phase field study of precipitate growth: effect of misfit strain and interface curvature, Acta Mater. 57 (13) (2009) 3947–3954.

[23] M. Faehrmann, E. Faehrmann, T.M. Pollock, O. Paris, P. Fratzl, An Experimental Study of the Role of Plasticity in the Rafting Kinetics of a Single Crystal Ni-base Superalloy, Superalloys 1996, Champion, Pennsyslvania; USA, 1996, pp. 191–200.

[24] T.M. Pollock, R.D. Field, Chapter 63 Dislocations and high-temperature plastic deformation of superalloy single crystals, in: Dislocations in Solids, 11, 2002, pp. 547–618.

[25] T. Furuhara, T. Maki, Variant selection in heterogeneous nucleation on defects in diffusional phase transformation and precipitation, Mater. Sci. Eng., A 312 (1–2) (2001) 145–154.

[26] M. Kato, S. Onaka, T. Fujii, Energy consideration for variant selection in precipitation on dislocations, Sci. Technol. Adv. Mater. 2 (2) (2001) 375–380.

[27] D. Qiu, R. Shi, D. Zhang, W. Lu, Y. Wang, Variant selection by dislocations during α precipitation in α/β titanium alloys, Acta Mater. 88 (2015) 218–231.

[28] D. Qiu, P. Zhao, R. Shi, Y. Wang, W. Lu, Effect of autocatalysis on variant selection of α precipitates during phase transformation in Ti-6Al-4V alloy, Comput. Mater. Sci. 124 (2016) 282–289.

[29] R. Shi, Y. Wang, Variant selection during α precipitation in Ti–6Al–4V under the influence of local stress – a simulation study, Acta Mater. 61 (16) (2013) 6006–6024.

[30] Z.Q. Feng, Y.Q. Yang, B. Huang, X. Luo, M.H. Li, M. Han, M.S. Fu, Variant selection and the strengthening effect of S precipitates at dislocations in Al–Cu–Mg alloy, Acta Mater. 59 (6) (2011) 2412–2422.

[31] Y. Wang, H.-Y. Wang, L.-Q. Chen, A.G. Khachaturyan, Microstructural development of coherent tetragonal precipitates in magnesium-partially-stabilized zirconia: a computer simulation, J. Am. Ceram. Soc. 78 (3) (1995) 657–661.

[32] H. Choe, T. Terai, I. Miyazaki, S. Yamamoto, M. Yonemura, T. Fukuda, T. Kakeshita, Selection of cementite variants precipitated under magnetic field in ferrite matrix of an Fe-C alloy, ISIJ Int. 56 (9) (2016) 1652–1655.

[33] J. Khalil-Allafi, A. Dlouhy, G. Eggeler, Ni4Ti3-precipitation during aging of NiTi shape memory alloys and its influence on martensitic phase transformations, Acta Mater. 50 (17) (2002) 4255–4274.

[34] J. Michutta, C. Somsen, A. Yawny, A. Dlouhy, G. Eggeler, Elementary martensitic transformation processes in Ni-rich NiTi single crystals with Ni4Ti3 precipitates, Acta Mater. 54 (13) (2006) 3525–3542.

[35] S.K. Das, G. Thomas, The metastable phase Ni2Mo and the initial stages of ordering in Ni-Mo alloys, Phys. Status Solidi A 21 (1) (1974) 177–190.

[36] G. Van Tendeloo, Short range order considerations and development of long range order in different Ni-Mo alloys, Mater. Sci. Eng. 26 (2) (1976) 209–220.

[37] J.M. Oblak, D.F. Paulonis, D.S. Duvall, Coherency strengthening in Ni base alloys hardened by DO22 γ' precipitates, Metall. Trans. 5 (1) (1974) 143.

[38] M.G. Fahrmann, S.K. Srivastava, L.M. Pike, HAYNES 244 alloy – a new 760 °C capable low thermal expansion alloy, in: MATEC Web of Conferences, 14, 2014, p. 17004.

[39] J. Song, R. Field, M. Kaufman, Crystallography of grain boundary precipitates in a Ni-Mo-Cr-W low CTE alloy, J. Alloy. Comp. 702 (2017) 687–692.

[40] S.G. Kim, W.T. Kim, T. Suzuki, Phase-field model for binary alloys, Phys. Rev. 60 (6) (1999) 7186–7197.

[41] S. Gyoon Kim, W. Tae Kim, T. Suzuki, M. Ode, Phase-field modeling of eutectic solidification, J. Cryst. Growth 261 (1) (2004) 135–158.

[42] N. Moelans, B. Blanpain, P. Wollants, An introduction to phase-field modeling of microstructure evolution, Calphad 32 (2) (2008) 268–294.

[43] K. Ammar, B. Appolaire, G. Cailletaud, S. Forest, Combining phase field approach and homogenization methods for modelling phase transformation in elastoplastic media, European J. Comp. Mech. 18 (5–6) (2009) 485–523.

[44] Y. Gao, R. Shi, J.-F. Nie, S.A. Dregia, Y. Wang, Group theory description of transformation pathway degeneracy in structural phase transformations, Acta Mater. 109 (2016) 353–363.

[45] H. Zapolsky, S. Ferry, X. Sauvage, D. Blavette, L.Q. Chen, Kinetics of cubic-to-tetragonal transformation in Ni-V-X alloys, Philos. Mag. A 90 (1–4) (2010) 337–355.

[46] V. Vaithyanathan, C. Wolverton, L.Q. Chen, Multiscale modeling of θ' precipitation in Al–Cu binary alloys, Acta Mater. 52 (10) (2004) 2973–2987.

[47] S.P. Murarka, M.S. Anand, R.P. Agarwala, Diffusion of chromium in nickel, J. Appl. Phys. 35 (4) (1964) 1339–1341.

[48] T.-F. Chen, Y. Iijima, K.-i. Hirano, K. Yamauchi, Diffusion of chromium in nickel-base Ni-Cr-Fe alloys, J. Nucl. Mater. 169 (1989) 285–290.

[49] C.P. Heijwegen, Diffusion in the Binary Systems of Molybdenum with Nickel, Iron and Cobalt, Department of Chemical Engineering and Chemistry, Technische Hogeschool Eindhoven, 1973.

[50] C. Zener, Theory of growth of spherical precipitates from solid solution, J. Appl. Phys. 20 (10) (1949) 950–953.

[51] S.M. Allen, J.W. Cahn, A microscopic theory for antiphase boundary motion and its application to antiphase domain coarsening, Acta Metall. 27 (6) (1979) 1085–1095.

[52] D. Fan, L.Q. Chen, Computer simulation of grain growth using a continuum field model, Acta Mater. 45 (2) (1997) 611–622.

[53] K.S. Chan, Y.-D. Lee, Y.-M. Pan, First-principles computations of mechanical properties of Ni2Cr and Ni2Mo, Metall. Mater. Trans. A 37 (3) (2006) 523–537.

[54] J.F. Nye, Physical Properties of Crystals: Their Representation by Tensors and Matrices, 1st published in pbk. with corrections, Clarendon Press, Oxford [Oxfordshire], 1985, 1986.

[55] L. Nguyen, R. Shi, Y. Wang, M. De Graef, Quantification of rafting of γ' precipitates in Ni-based superalloys, Acta Mater. 103 (2016) 322–333.

[56] J. Song, R. Field, D. Konitzer, M. Kaufman, Development of grain boundary precipitate-free zones in a Ni-Mo-Cr-W alloy, Metall. Mater. Trans. A 48 (5) (2017) 2425–2434.

[57] J.D. Embury, R.B. Nicholson, The nucleation of precipitates: the system Al-Zn-Mg, Acta Metall. 13 (4) (1965) 403–417.

[58] P.N.T. Unwin, G.W. Lorimer, R.B. Nicholson, The origin of the grain boundary precipitate free zone, Acta Metall. 17 (11) (1969) 1363–1377.

[59] M. Wen, A. Barnoush, K. Yokogawa, Calculation of all cubic single-crystal elastic constants from single atomistic simulation: hydrogen effect and elastic constants of nickel, Comput. Phys. Commun. 182 (8) (2011) 1621–1625.

[60] P.L. Gould, Introduction to Linear Elasticity, third ed., Springer New York, New York, NY, 2013, 2013.